Identifying Carbon as the Source of Visible Single Photon Emission from Hexagonal Boron Nitride

Noah Mendelson,[1] Dipankar Chugh,[2] Jeffrey R. Reimers,[1,3] Tin S. Cheng,[4] Andreas Gottscholl,[5] Hu Long,[6,7,8] Christopher J. Mellor,[4] Alex Zettl,[6,7,8] Vladimir Dyakonov,[5] Peter H. Beton,[4] Sergei V. Novikov,[4] Chennupati Jagadish,[2,9] Hark Hoe Tan,[2,9] Michael J. Ford,[1] Milos Toth,[1,10] Carlo Bradac,[1,11] Igor Aharonovich[1,10]*

[1]School of Mathematical and Physical Sciences, University of Technology Sydney, Ultimo, New South Wales 2007, Australia.
[2]Department of Electronic Materials Engineering, Research School of Physics and Engineering, The Australian National University, Canberra, Australian Capital Territory, Australia
[3]International Centre for Quantum and Molecular Structures and Department of Physics, Shanghai University, Shanghai 200444, China.
[4]School of Physics and Astronomy, University of Nottingham, Nottingham NG7 2RD, UK
[5]Experimental Physics 6 and Würzburg-Dresden Cluster of Excellence, Julius Maximilian University of Würzburg, Würzburg, Germany.
[6]Department of Physics, University of California, Berkeley, CA, USA.
[7]Materials Sciences Division, Lawrence Berkeley National Laboratory, Berkeley, CA, USA.
[8]Kavli Energy NanoSciences Institute at the University of California and the Lawrence Berkeley National Laboratory, Berkeley, CA, USA.
[9]ARC Centre of Excellence for Transformative Meta-Optical Systems, Research School of Physics and Engineering, The Australian National University, Australian Capital Territory, Australia
[10]ARC Centre of Excellence for Transformative Meta-Optical Systems, University of Technology Sydney, Ultimo, New South Wales, Australia.
[11] Department of Physics & Astronomy, Trent University, 1600 West Bank Dr., Peterborough ON, K9J 0G2, Canada

*Igor.Aharonovich@uts.edu.au

Abstract:
Single photon emitters (SPEs) in hexagonal boron nitride (hBN) have garnered significant attention over the last few years due to their superior optical properties. However, despite the vast range of experimental results and theoretical calculations, the defect structure responsible for the observed emission has remained elusive. Here, by controlling the incorporation of impurities into hBN via various bottom-up synthesis methods and directly through ion implantation we provide direct evidence that the visible SPEs are carbon related. Room temperature optically detected magnetic resonance (ODMR) is demonstrated on ensembles of these defects. We perform ion implantation experiments and confirm that only carbon implantation creates SPEs in the visible spectral range. Computational analysis of the simplest 12 carbon-containing defect species suggest the negatively charged $V_BC_N^-$ defect as a viable candidate and predict that out-of-plane deformations make the defect environmentally sensitive. Our results resolve a long-standing debate about the origin of single emitters at the visible range in hBN and will be key to the deterministic engineering of these defects for quantum photonic devices.

Single defects in solids have become some of the most promising frontrunner hardware constituents of applications in quantum information technologies and integrated quantum photonics.[1] Significant effort has been devoted to isolate and deterministically engineer such defects in wide bandgap materials such as diamond and silicon carbide.[2, 3] This collective effort resulted in spectacular proof of principle demonstrations ranging from quantum networks to spin-photon interfaces,[3] while simultaneously and steadily leading to understanding the fundamental level structures of these defects.

Recently, hexagonal boron nitride (hBN) has emerged as a promising host material for defects which display ultra-bright single photon emission (SPE)[4, 5, 6, 7, 8]. They exhibit remarkable properties: a strong response to applied strain and electric fields (Stark shifts),[9, 10, 11] stability under high pressure and elevated temperatures,[12, 13] potential for resonant excitation above cryogenic temperatures,[14, 15, 16] and addressability via spin-selective optical transitions.[17, 18] Yet, despite the numerous experimental characterizations and in-depth theoretical attempts to model their possible crystalline structure,[6, 19, 20, 21, 22, 23] the nature of these defects remains unknown.

Part of the challenge stems from standard hBN bulk crystal synthesis *via* high pressure high temperature not being amenable to the deterministic control of impurity incorporation. This is aggravated by the induced impurities often segregating and forming regions of inhomogeneous defect concentration.[24] In addition, the two-dimensional, layered nature of hBN makes ion implantation difficult to control. These limitations have precluded identifying the exact origin of the single photon emission in the material.

Here, we address this problem by carrying out a detailed study surveying various hBN samples grown in different laboratories by metal-organic vapor phase epitaxy (MOVPE) and molecular beam epitaxy (MBE). We find compelling evidence that to observe photoluminescence from SPEs the inclusion of carbon atoms in hBN is required. By systematically growing samples with different carbon concentrations, we show that the carbon content determines whether the photoluminescence signal originates from an ensemble of emitters (high carbon concentration) or isolated defects (low carbon concentration). Defect ensembles are demonstrated to display room temperature optically detected magnetic resonance (ODMR). We carry out multi-species ion-implantation experiments on both MOVPE films and exfoliated hBN, showing that only carbon implantation creates SPEs and that the density of emitters scales directly with the implantation dose of carbon. Our results are supported by rigorous modelling analysis of carbon related defects.

HBN GROWTH

Table 1 summarizes the materials analyzed. They are epitaxial hBN samples grown by different methods and under various conditions. The rationale was to understand whether the single defects are intrinsic to hBN (e.g. substitutional or interstitial nitrogen or boron complexes) or they involve foreign atoms (e.g. carbon). We investigated hBN samples grown by four methods. 1) Metal organic vapor phase epitaxy (MOVPE) with varying flow rates of the precursor triethyl boron (TEB)—a parameter known to systematically alter the levels of incorporated carbon. 2) High temperature molecular beam epitaxy (MBE) on sapphire with and without a source of carbon. 3) High-temperature MBE on SiC with a varying orientation of the Si face to explore the possibility of carbon incorporation occurring from the substrate. 4) Growth by the conversion of highly oriented pyrolytic graphite (HOPG) into hBN. Note, that in the current work we focus on bottom up growth of hBN as it offers an opportunity for large (centimeter) scale films of desired thickness (down to ~1 nm), as well as better control over the inclusions of impurities.

| Sample	Abbreviation	Growth Method & Details	SPE Photoluminescence	Additional Info
MOVPE hBN (TEB flux 10)	MOVPE hBN (TEB 10)	MOVPE on Sapphire, Precursors (triethyl borane & ammonia) TEB flow 10 µmol/min, H_2 carrier gas, 1350˚C	Isolated SPEs, ZPLs Predominantly ~585±10 nm	~40 nm thick
MOVPE hBN (TEB flux 20)	MOVPE hBN (TEB 20)	MOVPE on Sapphire, Precursors (triethyl borane & ammonia) TEB flow 20 µmol/min, H_2 carrier gas, 1350˚C	Dense and Uniform Ensemble of SPEs with ZPL ~585, PSB ~630.	~40 nm thick
MOVPE hBN (TEB flux 30)	MOVPE hBN (TEB 30)	MOVPE on Sapphire, Precursors (triethyl borane & ammonia) TEB flow 30 µmol/min, H_2 carrier gas, 1350˚C	Dense and Uniform Ensemble of SPEs with ZPL ~585, PSB ~630.	~40 nm thick
MOVPE hBN (TEB flux 60)	MOVPE hBN (TEB 60)	MOVPE on Sapphire, Precursors (triethyl borane & ammonia) TEB flow 60 µmol/min, H_2 carrier gas, 1350˚C	Dense and Uniform Ensemble of SPEs with ZPL ~585, PSB ~630.	~40 nm thick
MBE hBN on Sapphire	Undoped MBE hBN on sapphire	MBE on sapphire, Boron flux from e-beam source (300W). Boron in BN crucible. Nitrogen flow 2sccm. Growth temperature 1250˚C.	No SPEs Present	~20 nm thick
MBE hBN on Sapphire with Carbon Crucible	Carbon doped MBE hBN on Sapphire	MBE on sapphire, Boron flux from e-beam source (210W). Boron in carbon crucible. Nitrogen flow 2sccm. Growth temperature 1250˚C.	Semi-Isolated SPEs, ZPLs Range from 570-770 nm, Density ~5-8/µm²	~18 nm thick
MBE hBN on Silicon Carbide (0˚ Si Face)	Undoped MBE hBN on SiC (0˚)	SiC (Si-face, orientation-on) MBE on SiC. Boron flux from HT Knudsen source at 1875˚C. Nitrogen flow 2sccm. Growth temperature 1390˚C.	Very Few SPEs Density ~1 SPE in 40µm²	~3 nm thick
MBE hBN on Silicon Carbide (8˚ Si Face)	Undoped MBE hBN on SiC (8˚)	SiC (Si-face, orientation 8˚-off) MBE on SiC. Boron flux from HT Knudsen source at 1875˚C. Nitrogen flow 2sccm. Growth temperature 1390˚C.	Isolated SPEs, ZPLs Range from 575-735 nm Density ~3-5/µm²	~7 nm thick
HOPG→hBN Conversion	Converted hBN	HOPG is placed in a radio frequency induction furnace at 2000˚C, N_2 gas is mixed with thermalized B_2O_3 powder facilitating conversion	Dense and Uniform Ensemble of SPEs with ZPL ~580, PSB ~630.	Bulk

Table 1—Epitaxial hBN Samples with Varying Carbon Concentrations. *The 9 different hBN sample types used in the study, their growth methods, and SPE characteristics. Color coding correlates with the growth method.*

We first explore the photoluminescence (PL) from a series of hBN samples grown by MOVPE[25] as the triethyl boron (TEB) flow rate is increased and the ammonia flow is kept constant shown in Figure 1a. The aim of this measurement is to engineer an ensemble of hBN emitters, and to compare their properties with isolated SPEs grown using the same growth technique. A region of the TEB 10 (µmol/min) sample with the lowest percentage of carbon shows negligible fluorescence. Increasing the flow rate to TEB 20 is accompanied by the appearance of a bright fluorescence signal with two clear peaks appearing at ~585 nm and ~635 nm. Further increasing the flow rate to TEB 30 and 60 provides a similarly structured PL signature, with higher fluorescence intensity, confirming that higher PL intensity directly correlates with higher TEB flux. Moderate fluctuations in the peak positions, and intensity ratio of the 585 nm and 635 nm peaks at different sample locations are consistent with emission from dense ensembles of hBN emitters. This also confirms previous findings showing that hBN emitters possess zero-phonon line (ZPL) wavelengths clustered at ~585 nm when the sample is grown epitaxially.[26, 27] The energy detuning between the ZPL of the ensemble and phonon sideband (PSB) peak is ~176 meV on average.[28, 29]

Figure 1b(c) demonstrate near linear correlations between C-B (C-N) bonding and increasing TEB flux, with C-B bonding being roughly an order of magnitude more prevalent than C-N bonding. Preferential formation of C-B bonds follows logically from noting the B species are introduced with three pre-existing bonds to C. PL intensity of the resulting ensemble emission likewise displays a linear correlation with carbon concentration, see supporting information. Based

on these results, we advance that the SPE emission at ~580 nm in hBN is likely to originate from a carbon-related defect complex.
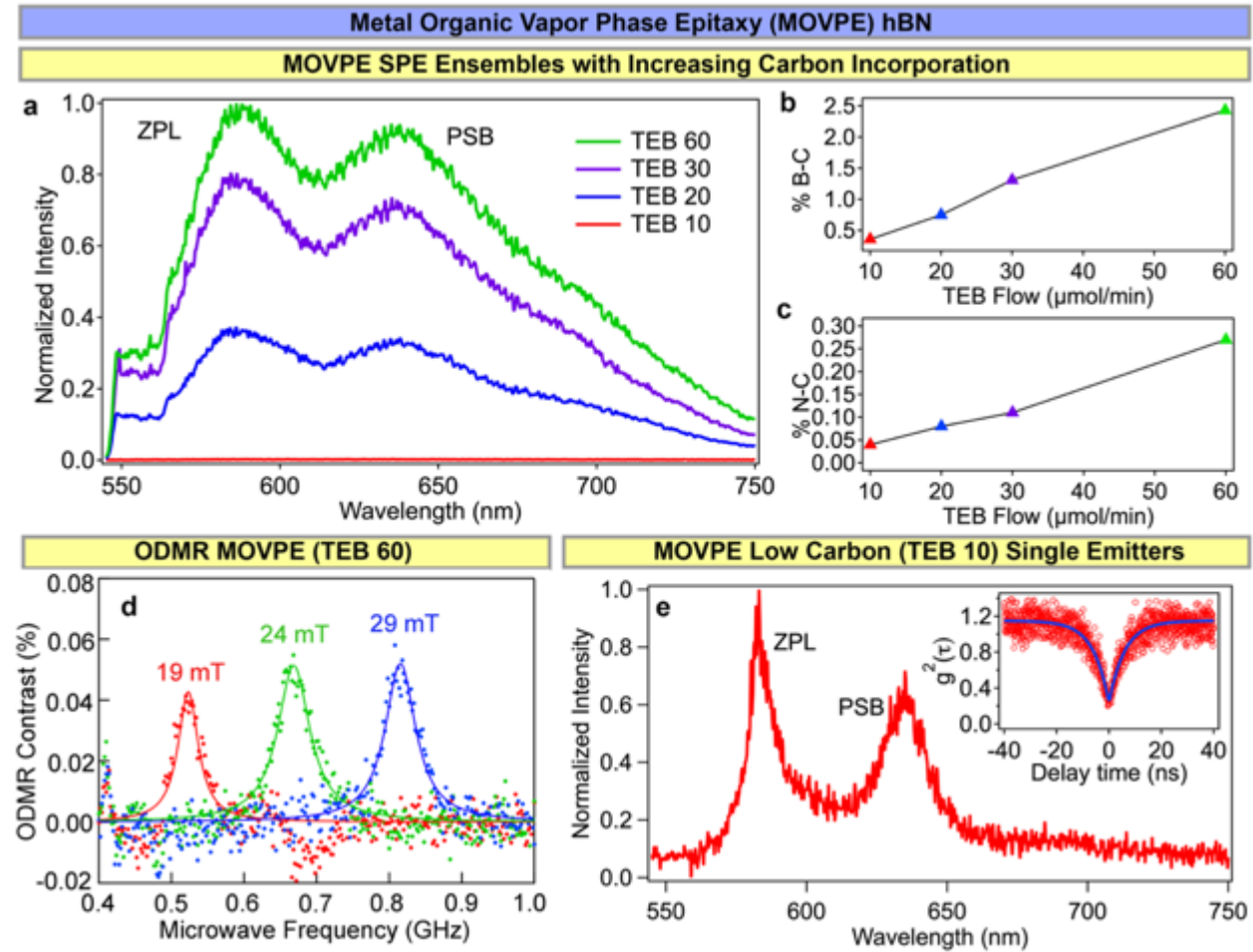
Figure 1—Photoluminescence from MOVPE hBN Samples. *a. MOVPE hBN grown with increasing flow rates of triethyl borane (TEB). As TEB flow increases, the fluorescence of SPE ensembles increases.* ***b.*** *Percentage of B-C bonding with increasing TEB flow evaluated by XPS.* ***c.*** *Percentage of N-C bonding with increasing TEB flow evaluated by XPS.* ***d.*** *Room temperature ODMR contrast observed from the ~585 nm ensemble emission of MOPVE hBN (TEB 60) at applied fields of 19, 24, and 29 mT respectively.* ***e.*** *Spectrum of a representative SPE found in MOVPE hBN TEB 10. Inset displays the corresponding autocorrelation measurements from the spectrum.*

Figure 1d shows the ODMR spectra recorded from the TEB 60 sample. The highly symmetric shape of the signal does not reveal a structure that would allow a clear assignment to a specific intrinsic or extrinsic defect. However, it is clearly a spin-carrying defect , likely with a spin state higher than S=1/2. By varying the static magnetic field B, we measure resonances at ~523, ~668.5 and ~815.4 MHz for B = 19, 24 and 29 mT, respectively. A value for g_e of ~2.09 is extracted, as shown in the supporting information. However, we observe no splitting of the signal with the magnetic field, which means that the zero-field splitting, *D*, should be small. In previous experiments, a similar ODMR signal was observed at low temperature (T=8.5 K),[18] while our measurements show that ODMR is also feasible at room temperature. In both experiments the

linewidths were identical and mostly temperature independent (see SI). The line-broadening may be due to dipole-dipole coupling, e.g. by hyperfine interaction with nearby nuclei, rather than a relaxation time mechanism. This is consistent with the preliminary assignment that the ODMR signal measured on the heavily carbon-doped sample and shown in Fig. 2d is associated with a carbon-related defect.[18]

We next employ a lab-built confocal PL setup with a 532 nm excitation source, to study in detail the TEB 10 sample. The level of carbon doping is such that we can isolate single quantum emitters; a representative spectrum for one such emitter is shown in Figure 1d. The quantum nature of the emission was confirmed by measuring the second order auto-correlation function; the value of $g^{(2)}(\tau = 0) < 0.5$ (Fig. 1d inset) is conventionally attributed to a single photon source with sub-Poissonian emission statistics. We measured the zero-phonon line (ZPL) wavelength of 77 SPEs in the MOVPE hBN (TEB 10) sample, finding that ~78% of the emitters are located at (585 ± 10) nm, and 95% at wavelengths < 600 nm , consistent with previous studies on epitaxially grown hBN.[26, 27] The typical line shape of these emitters at room temperature is also consistent with previous studies, including the ZPL and a PSB centered at ~177 meV from the ZPL energy. This suggests that when the carbon concentration is sufficiently low, individual quantum emitters can be isolated. Their optical properties and spectral distribution are consistent with those observed in samples with higher carbon doping, with the difference merely being due to the density of emitters.

To further confirm that carbon-based defects are responsible for SPE emission from hBN we analyze a series of hBN samples grown by a different method, high-temperature MBE.[30, 31] Figure 2a displays the PL spectrum observed from undoped MBE hBN grown on sapphire substrate. The resulting PL signal was relatively low; no SPEs could be found despite the material being of good quality as shown by a clear hBN E_{2g} Raman line. However, when the elemental boron source was placed inside a carbon crucible—with otherwise identical growth conditions—we observed the appearance of sharp spectral lines, shown in figure 2b. The carbon crucible used for e-beam evaporation of the boron shows clear signs of sidewall etching, which suggests that carbon was present in the gas phase during growth.

The MBE growth resulted in a high density emitters that we could not isolate at single sites.. We instead probed the polarization dependence of the emission by placing a polarizer in the collection path. Figure 2c shows one such collection, where emission from a presumed ZPL at ~577 nm is linearly polarized, with the PL intensity dropping when the polarizer is perpendicular to the polarization direction of the probed emitter.
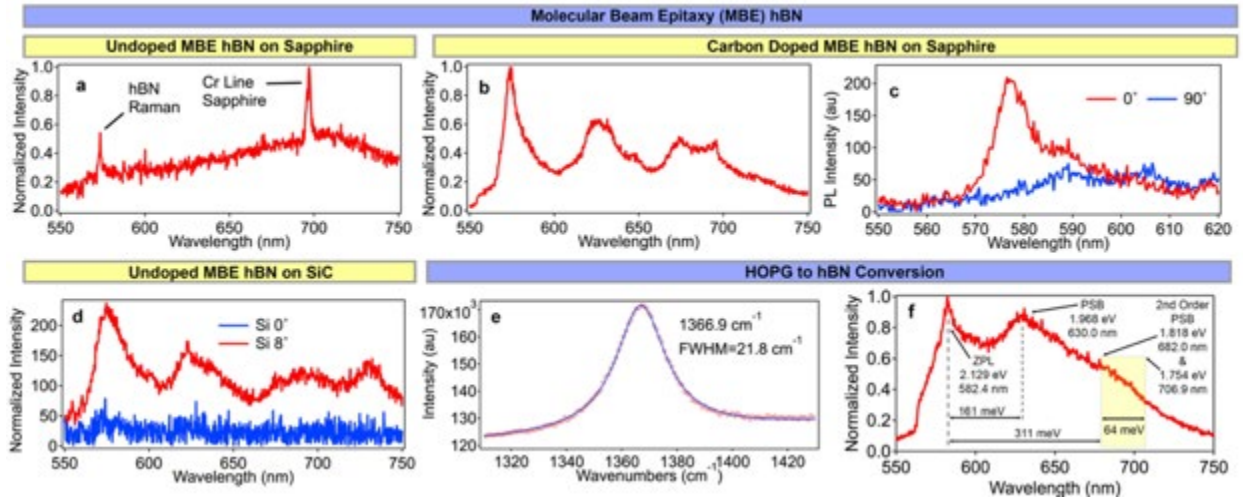
Figure 2—Photoluminescence from MBE and HOPG Conversion hBN Samples. a. *Undoped MBE hBN on sapphire displays no SPEs.* ***b.*** *Carbon doped MBE hBN on sapphire displaying a number of isolated peaks spanning the visible range. Typically, many SPEs are found within the laser excitation spot.* ***c.*** *Polarization resolved photoluminescence of a single peak in carbon doped MBE hBN on sapphire (b), demonstrating the polarized nature of the emission.* ***d.*** *Undoped MBE hBN on silicon carbide, with the Si face oriented at 0˚ (blue) and 8˚ off (red). While growth of the Si 0˚ face SiC shows no SPEs, growth on the Si 8˚-off face effectively incorporates SPEs via diffusion of C from the SiC substrate.* ***e.*** *Raman spectra of the HOPG to hBN conversion sample.* ***f.*** *Converted hBN displays an SPE ensemble emission centered around ~585 nm.*

We next explored MBE growth of hBN on silicon carbide (SiC), investigating different crystal orientations: specifically, with the top Si face-on (0˚) and slightly off (8˚). Representative spectra from both sample types (Si at 0˚ and at 8˚) are displayed in Figure 2d. When growth was performed with the Si face at 0˚, only a single SPE peak was located across a 40 μm^2 scan. In contrast, when the Si face is oriented at 8˚ we found a number of SPE peaks across the sample, often with a number of different ZPL wavelengths appearing within the same confocal spot. The incorporated SPEs display a similar ZPL distribution to the carbon doped MBE hBN on sapphire (see SI), at a slightly lower density.

We attribute the incorporation of these SPEs during hBN growth on SiC to carbon diffusion from the substrate. At the growth temperature of 1390 ˚C, some sublimation of Si from the surface of the SiC substrates is expected, with the subsequent formation of an extra carbon layer on the surface of SiC.[32] While these temperatures are sufficient to sublime Si, they are not sufficient to evaporate C from the SiC surface.[32] Interestingly, C incorporation into hBN appears significantly enhanced when the Si face is oriented 8˚ out of plane. The observed dependence of SPE incorporation during MBE growth further support the role of carbon in the origin of hBN SPEs in the visible spectral range.

Finally, we analyze a third technique for hBN growth, the conversion of HOPG to hBN, known to yield high quality porous hBN.[33] Conversion was confirmed by Raman spectroscopy (Figure 2e).[34] The conversion from graphite, proceeding via atomic substitutions, provides a high availability of carbon for incorporation as defects in the resulting hBN. Figure 2f displays a typical PL spectrum from the sample. We observe a bright and structured emission with ZPL and PSB peaks displaying similar transition energies as observed for high carbon MOVPE ensembles.

Figure 3—MOVPE hBN (TEB 10) Samples Implanted with Carbon. *Implantations were done at a dose of 10^{13} cm^{-2} and an energy of 10 keV, using a TEM grid with 50 μm^2 apertures as a mask. **a**. Confocal scan of carbon implanted sample, where square areas marked (I) were implanted, and those marked (II) were masked. **b**. Spectra from implanted areas (I) display narrow ZPLs with almost no PSB and are attributed to emitters created via implantation. A representative $g^{(2)}(\tau)$ is shown to the right. **c**. Spectra and $g^{(2)}(\tau)$*

Carbon Implanted MOVPE hBN

Pre-Anneal

Annealed (1000°C, Hi-Vac, 2 hours)
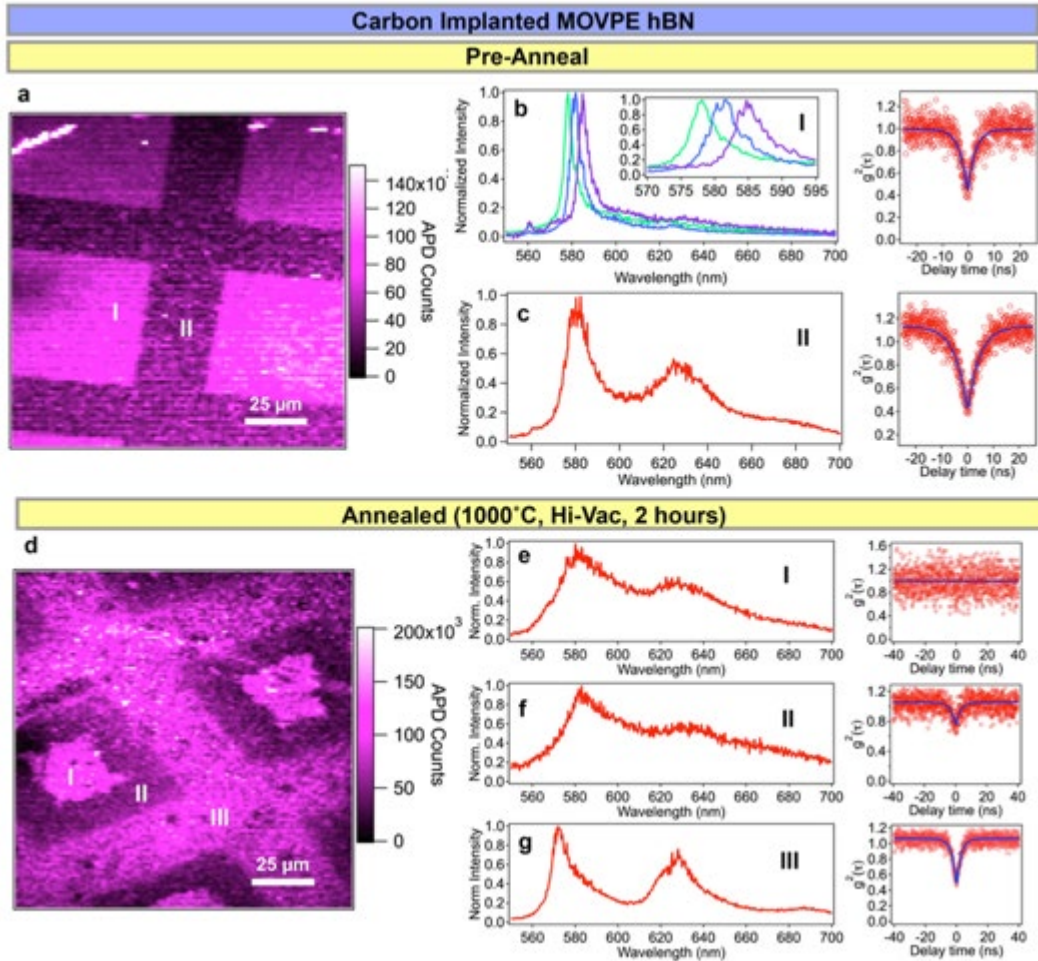
*from the masked area (II) display borderer ZPLs, and prominent PSBs. **d**. Confocal scan of the carbon implanted sample, post annealing, where areas marked (I) and (II) were implanted, while area (III) was masked. **e**. A representative spectra and $g^{(2)}(\tau)$ from area (I), showing an ensemble of hBN emitters, and a corresponding $g^{(2)}(\tau)$ measurement showing no dip as expected for ensemble emission. **f**. A representative spectra and $g^{(2)}(\tau)$ from area (II) showing evidence of quantum emission but with significant spectral contributions from nearby SPEs resulting in a $g^{(2)}(\tau)$ value of ~ 0.75. **g**. A representative spectra and $g^{(2)}(\tau)$ from the masked area (III) post annealing showing a well-resolved SPE and PSB and a $g^{(2)}(\tau)$ confirming a single emission center.*

ION IMPLANTATION

We now turn our attention to using ion implantation for defect creation, in an attempt to confirm the role of carbon. We performed a series of implantation experiments (dose: 10^{13} ions/cm^{-2}, energy 10 keV) with carbon as well as silicon and oxygen used as controls to rule out the possibility for the photoemission to be due to native vacancy defects. The implantation experiments were performed on the MOVPE hBN (TEB 10) films to compare the relevant results to those for the samples synthesized while increasing carbon content during growth.

Figure 3a shows the confocal scan of the TEB 10 sample after carbon implantation, but prior to annealing, where a TEM grid with 50 μm^2 square apertures was used as a mask. The implanted region is labelled I, while the masked region is labelled II. Figure 3b displays spectra collected from emitters within the implanted region (I), and a representative $g^{(2)}(\tau = 0) < 0.5$, confirming the quantum nature of the emission from these centers. Figure 3c displays a representative emitter from the masked region (II), showing the typical line shape of the ZPL and the PSB peaks found in TEB 10 films, with the corresponding $g^{(2)}(\tau = 0)$ shown to the right.

Inside the C-implanted region, most emitters (~ 80%) display narrow ZPL peaks (~5 nm FWHM) and extremely weak PSBs, compared to the typical ZPL/PSB found in these TEB 10 films.. The remaining ~20% of SPEs within the implanted region display similar line shapes and phonon coupling to those for the emitter in figure 3c and are attributed to preexisting SPEs in the region. Our results indicate that the sharp emission lines belong to SPEs created via implantation of C ions. The reasons for the observed narrow line shape and the minimal phonon coupling are explored further *via* computational modelling below.

The samples were then annealed in high vacuum (1000 ˚C, <10^{-6} Torr, 2 hours), and the same set of measurements was performed. As shown in figure 3d, the implanted regions are still visible, they however show variations in PL intensity. This effect is likely due to ion scattering around the mask edges and vacancy diffusion—which have been observed for implantation in diamond.[35] The PL spectra from three different areas are shown in figure 3e–f, and correspond to (I) the implanted region of high PL intensity, (II) the implanted region of lower PL intensity, and (III) the masked region of the film.

Figure 3e displays a representative spectrum from inside region I, where we found broad emission similar to those observed in the high TEB flux growths. This emission is confirmed to be due to an ensemble of SPEs as the corresponding $g^{(2)}(\tau)$ measurements show no anti-bunching despite the associated ZPL/PSB structure. A similar spectral signature is observed consistently throughout region (I), again implying the creation of an ensemble of C-based SPEs. Figure 3f displays a representative spectrum from the implanted region II, where we again observe luminescence with a similar line shape. The overall ensemble signal remains homogeneous in this region, although appears less dense and bright, and the $g^{(2)}(\tau)$ measurement shows a value of ~0.75, confirming the presence of fewer emitters within a confocal spot. Note that in both implanted areas (I and II) we no longer find the narrow emission lines with low phonon coupling found prior to annealing. Finally, figure 3g displays a representative spectrum from region III (masked area), showing a typical ZPL and PSB profile with a $g^{(2)}(0) < 0.5$. Control experiments implanting silicon and oxygen with otherwise identical conditions were also performed, but the emitters, either singles or ensembles were not observed (see SI for details).

To further study SPE formation via ion implantation we performed dose dependent experiments with carbon fluences over the range 1×10^{11}-10^{14} ions/cm^2, while oxygen and silicon implantation at 1×10^{13} ions/cm^2 served as a control. Both MOVPE (TEB 10) hBN and exfoliated pristine hBN flakes (HQ Graphene) were used. The samples were subsequently annealed at 1000

°C in high vacuum conditions and analyzed via wide field imaging, which allowed for a direct visualization of the resulting SPE density.

Figure 4a shows representative images from the exfoliated hBN flakes before and after annealing. The results demonstrate unambiguously that emitter creation scales with the dose of carbon implantation in both cases, which directly confirms the creation of SPEs. Only a few emitters are formed without annealing even at higher doses, but the increasing trend of emitter formation is clearly evident after annealing.

Figure 4b shows a direct comparison for carbon, oxygen and silicon ion implantations at a dose of 1×10^{13} ions/cm^2. As expected, for the MOVPE samples that contain residual carbon, the emitter density is high for both oxygen and silicon ions, and even higher for the carbon ions. This is because all ions create vacancies which is indicative of them being involved along carbon in the defect structure. However, in the exfoliated samples, only the carbon implantation results in the direct formation of single emitters at a high density. The implantation with oxygen or silicon does not yield any localized emitters. Figure 4c shows two spectra recorded from the localized emission spots in the carbon implanted exfoliated samples, before and after annealing. Green and red circles in figure 4a mark the position of the recorded spectra in each case. Additional spectral characterization is given in the SI.

In light of the implantation results, we briefly consider a potential ancillary role of carbon. This could occur through the stabilization or charge state modification of alternative defects, as well as modification of the material Fermi level. Critically, our implantation results allow us to rule out these possibilities. The creation of SPEs prior to annealing with C implantation only (i.e. not with Si and O implantation), despite clear evidence of increased vacancy creation excludes the secondary role of carbon as that of simply *activating* native vacancy complexes. Furthermore, complex native defects (e. g. $V_N N_B$) or non-carbon heteroatom impurities involving O and Si are similarly inconsistent with our results.. Note also that the dose dependent implantation experiments conclusively demonstrate that the density of created SPEs scales with the fluence of C ions in high purity hBN materials.
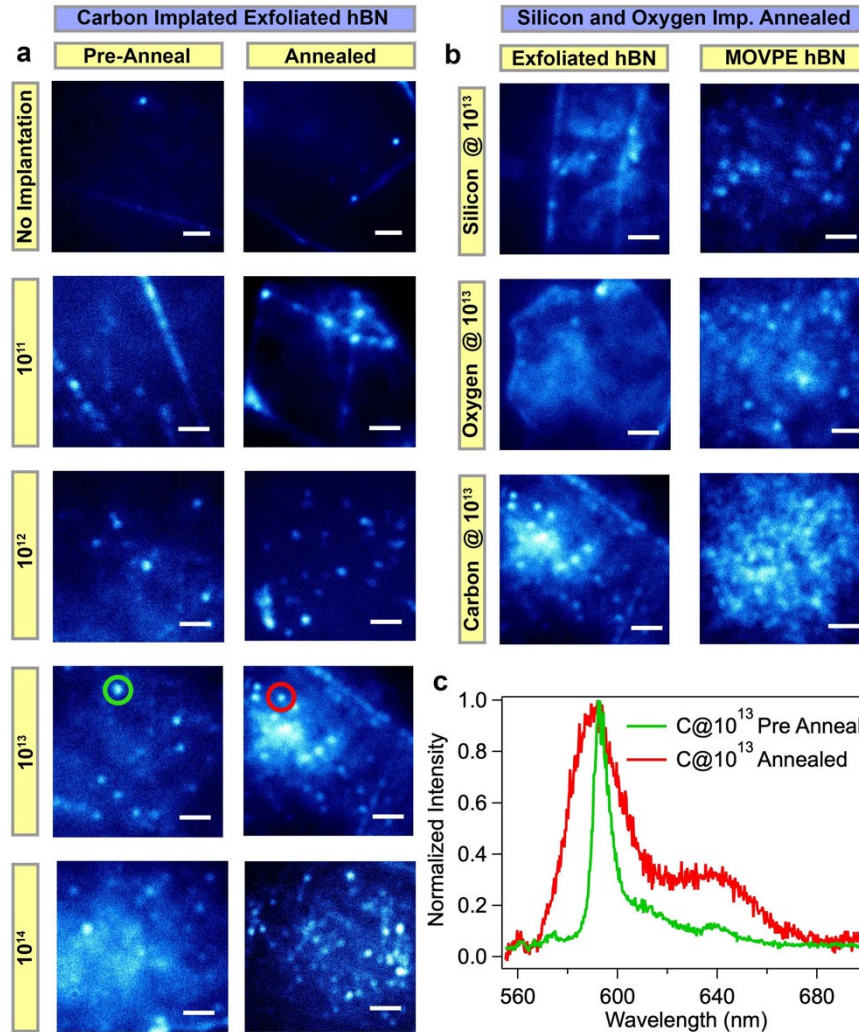
Figure 4—Wide field Imaging of Ion Implanted MOVPE and Exfoliated hBN. *Scale bars in each case are 2 µm.* ***a.*** *Exfoliated hBN samples for a series of carbon implanted samples with increasing fluences from 10^{11}-10^{14} ions/cm^2. Isolated bright spots (corresponding to SPEs) increase with the dose of carbon implantation.* ***b.*** *MOVPE (TEB 10) and exfoliated hBN samples implanted with carbon oxygen and silicon implanted samples at a fluence of 10^{13} ions/cm^2. SPE formation is the same with and without O and Si implantation but increases upon C implantation.* ***c.*** *Spectra from carbon implanted exfoliated hBN before and after annealing. Red and green circles in panel a identify the position in which the spectrum was recorded.*

ELECTRONIC STRUCTURE CALCULATIONS

To gain further insight into the structure of the carbon defect, we searched for defect transitions from which the observed photoemission could originate. To do so, time-dependent density-functional theory[38] (TD-DFT) calculations were performed using the CAM-B3LYP[39] density functional, (see Supporting Information for extensive details). These are supported by calculations using the HSE06 density functional[40] and the advanced equation-of-motion coupled cluster singles and doubles (EOM-CCSD)[41] methods. Four main defect candidates were considered: C_B, C_N, V_NC_B, and V_BC_N (Figure 5a-d) in their neutral, negative (−1), and positive (+1) charged states. Two spin manifolds were considered for each (either singlet and triplet or else

doublet and quartet), as well as at least ten excited states of each type. Calculations were performed using 3-ring, 5-ring, and 10-ring model compounds containing 1 or 3 hBN layers, to account for the effects of the host matrix on the defect. Figure 5e displays the 3-ring, 1-layer and 3-layer, model for V_BC_N-. Calculations on 10-ring systems were performed using a mixed quantum-mechanics / molecular-mechanics (QM/MM) scheme, utilizing an AMBER[42] potential fitted to mimic CAM-B3LYP results on 5-ring h-BN.

Given the large number of possible defect candidates considered we proceeded by eliminating unsuitable ones by combining our calculations to known experimental data. We focused on three well established experimental features of the SPEs, a ZPL energy transition of ~ 2.1 eV,[26, 27] a fast excited state lifetime of ~2-6 ns, [7] and a high quantum efficiency.[43] Accordingly, computational results were filtered to reproduce first, a CAM-B3LYP-calculated lowest-energy transition of 1.6 – 2.6 eV (based on the expected *worst-case* computational error, calibrated for this method to be ±0.5 eV),[22] and second, an oscillator strength exceeding 0.1, compatible with the observed short photoluminescence lifetime and high quantum yield. Few defects have lowest transition energies in this range, and most transitions are predicted to have oscillator strengths one hundredth of this or much less. Based on these considerations, only two candidates remain of interest amongst the options considered: the $(1)^4B_1 \rightarrow (1)^4A_2$ transition in $V_BC_N^-$, and the $(2)^3B_1 \rightarrow (1)^3B_1$ transition in V_NC_B. Of these, V_NC_B is immediately illuminated as its spectral bandshape and most other properties are highly inconsistent with observed features; hence we focus on $V_BC_N^-$.
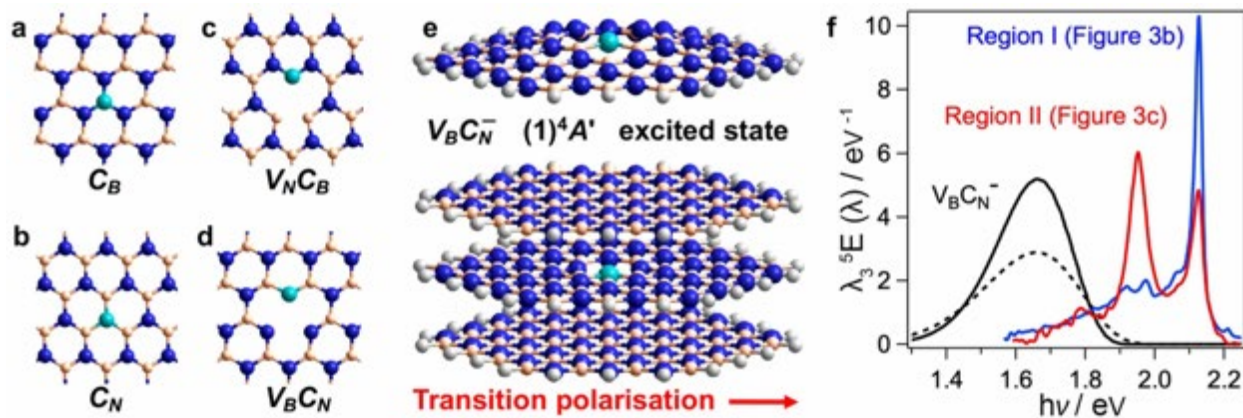
Figure 5—Computational Modelling. *Properties were determined for defects in their neutral and ±1 charged states. Indicative high-symmetry defect structures are shown in **(a)-(d)** (N- blue, B- peach, C-cyan): **(a)** for C_B^+, C_B^-, C_B; **(b)** for C_N^+, C_N^-, C_N; **(c)** for $V_NC_B^-$, $V_NC_B^+$, V_NC_B; and **(d)** for $V_BC_N^-$, $V_BC_N^+$, V_BC_N. It is concluded that the only feasible emission source is the $(1)^4B_1 \rightarrow (1)^4A_2$ transition in $V_BC_N^-$, with fully optimized 3-ring 1-layer and 3-ring 3-layer structures shown in **(e)**, along with the allowed in-plane-perpendicular electric polarization vector. In **(f)**, its predicted band shape (black dashed: basic CAM-B3LYP 3-ring 1-layer model, black solid: QM/MM EOM-CCSD 10-ring 3-layer out-of-plane distorted model) is compared to observed ones from Region I (blue, Fig. 3b C-Implanted) and Region II (red, Fig. 3c masked). The observed spectra are shown after correction for instrument response functions and converted from raw emission $E(\lambda)$ to bandshape $\lambda^5 E(\lambda)$ plotted versus energy $hv = hc/\lambda$, displaying broadening to a resolution of 0.01 eV. The predicted spectra are both too low in energy and too broad than the experimental ones, but the assignment is within computational uncertainty.*

The ground state of $V_BC_N^-$ is predicted to be $(1)^4A_2$, with unpaired electrons in a_1 (σ), b_1 (π) and b_2 (σ) orbitals. Four low-energy excited states are predicted, of which the lowest-energy one would need to be $(1)^4B_1$. One-layer models predict that this state undergoes out-of-plane distortion which lowers the energy. The distortion however can be either removed or enhanced once multi-layer models are considered. This transition has dominant $a_1(\sigma) \rightarrow b_2(\sigma)$ character, polarised in-plane and perpendicular to the defect's C_{2v} axis (see Figure 5e), with an oscillator strength exceeding 0.1. Figure 5f compares calculated emission bandshapes $E(\nu)/\nu^5$ (obtained as the raw emission scaled by wavelength to the 5th power) with calculated ones. The $(1)^4B_1 \rightarrow (1)^4A_2$ emission is predicted to be slightly lower in energy and much broader. The calculated width is environment dependent (Figure 5f) and dominated by how the calculations perceive torsional changes at the defect associated with light emission that generate low-frequency phonons. The observed spectra in Region I are indicative of such effects, but their magnitude is reduced to one third. The observed spectra in Region II are very different, primarily manifesting the effects of activation of BN-stretch phonons instead. It could be that the perceived sensitivity of $V_BC_N^-$ photoemission to local environment can account for the stark contrast in the observed spectra (Figure 5f).

The most significant shortcoming of the proposal of this defect as the dominant hBN SPE would be that intense absorption is predicted in only one polarization, whereas experiments suggest that higher-energy absorptions exist with alternate polarization. Of the 24 defect manifolds considered herein, it is the only one to remain of interest. More complex carbon-cluster defects have been previously considered as alternatives[44] without success, but a preprint has just appeared[JARA arXiv] suggesting two such possibilities: C_2C_N and C_2C_V. Preliminary calculations indicate similar strengths and weakenesses as for $V_BC_N^-$, overestimating reorganization energies and spectral widths whilst only allowing for absorption in one polarization.

In summary, we have presented rigorous experimental results to confirm the central role of carbon in hBN quantum emitters in the visible spectral range. We compared samples grown by MOVPE, MBE, and HOPG conversion. All methods exhibited a direct correlation between the introduction of carbon as a precursor/substance and the formation of SPEs. Furthermore, MOVPE growth enabled us to deterministically control carbon incorporation and vary the density of the quantum emitters from singles to ensembles and observe room temperature ODMR. We have also generated SPEs using direct ion implantation of carbon, and showed that their density scales with the implantation dose. Employing a TD-DFT method, we proposed the negatively charged V_BC_N- as a suitable transition to explain the observed results. Our results will accelerate the deployment of visible quantum emitters in hBN into quantum photonic devices and will advance potential strategies for the controlled engineering of quantum emitters in van der Waals crystals.

Methods

Metal Organic Vapor Phase Epitaxy. hBN layers were grown on commercially available 2" sapphire substrates using metal organic vapor phase epitaxy (MOVPE), as described in.[25] Triethyl boron (TEB) and ammonia were used as the boron and nitrogen precursors, respectively, while hydrogen was the carrier gas. The precursors were introduced into the reactor as short alternating pulses, in order to minimize parasitic reactions between TEB and ammonia. hBN growth was carried out at a reduced pressure of 85 mBar and the growth temperature was set to 1350°C. In the present study, the TEB flux was varied from 10 μmol/min to 60 μmol/min to study the effect on carbon incorporation on sub-bandgap luminescence from the hBN films. For ion implantation, PL and SPE measurements, cm-sized hBN films were transferred from sapphire on to SiO_2/Si substrates, using water-assisted self-delamination.[25] Thickness of the hBN films was also measured using atomic force microscopy, as shown in the supplementary information. X-ray photoelectron spectroscopy was used for determining the impurity levels in the as-grown MOVPE-hBN films, as shown in the supplementary information. A gentle etching using Ar beam was performed in-situ to remove adventitious carbon and impurities from the surface; all spectra were collected from the bulk of hBN films.

Molecular beam epitaxy. BN epilayers were grown using a custom-designed Veeco GENxplor MBE system capable of achieving growth temperatures as high as 1850 °C under ultra-high vacuum conditions, on rotating substrates with diameters of up to 3 inches. Details of the MBE growth have been previously published.[30] In all our studies, we relied on thermocouple readings to measure the growth temperature of the substrate. For all samples discussed in the current paper the growth temperature was in the range 1250–1390 °C. We used a high-temperature Knudsen effusion cell (Veeco) or electron beam evaporator (Dr. Eberl MBE-Komponenten GmbH) for evaporation of boron. High-purity (5 N) elemental boron contains the natural mixture of ^{11}B and ^{10}B isotopes. To contain boron in the e-beam evaporator we used boron nitride and vitreous carbon crucibles. We used a conventional Veeco RF plasma source to provide the active nitrogen flux. The hBN epilayers were grown using a fixed RF power of 550 W and a nitrogen (N_2) flow rate of 2 sccm. We used 10×10 mm^2 (0001) sapphire and on- and 8°-off oriented Si-face SiC substrates. Variable angle spectroscopic ellipsometry (VASE) provided the thickness of the hBN layers.

HOPG to hBN Conversion. The conversion takes place in a graphite crucible. A HOPG crystal is placed in the center of the crucible on a separate graphite holder. Small holes in the stage holding the HOPG allow vapors from the boron-oxide powder, placed at the bottom of the crucible, to flow to the HOPG crystal. A radio frequency induction furnace is then heated to 2000 °C, and N_2 gas is introduced as the nitrogen precursor. A central tube mixing the nitrogen gas with the boron-oxide vapor pre-mixes the precursors prior to arriving at the HOPG crystal. Further details can be found here.[33]

Ion Implantation. Ion implantation was carried out on 40 nm-thick MOVPE-hBN films, grown using a TEB flux of 10 μmol/min. For this, the hBN films were first transferred on to SiO_2/Si

substrates. A copper grid with a square mesh (GCu300, ProSciTech) was used as the implantation mask. Carbon, silicon and oxygen were separately implanted into the hBN films. During implantation, the ion energy and fluence were 10 keV and 10^{13} ion/cm^2, respectively.

Confocal Microscopy. PL studies were carried out using a lab-built scanning confocal microscope with continuous wave (CW) 532-nm laser (Gem 532, Laser Quantum Ltd.) as the excitation source. The laser was directed through a 532 nm line filter and a half-waveplate and focused onto the sample using a high numerical aperture (100×, NA = 0.9, Nikon) objective lens. Scanning was performed using an X−Y piezo fast steering mirror (FSM-300). The collected light was filtered using a 532-nm dichroic mirror (532 nm laser BrightLine, Semrock) and an additional 568-nm long pass filter (Semrock). The signal was then coupled into a graded-index multimode fiber (fiber aperture of 62.5 μm). A flipping mirror was used to direct the emission to a spectrometer (Acton Spectra Pro, Princeton Instrument Inc.) or to two avalanche photodiodes (Excelitas Technologies) in a Hanbury Brown-Twiss configuration, for spectroscopy and photon counting measurements, respectively. Correlation measurements were carried out using a time- correlated single photon counting module (PicoHarp 300, PicoQuant). All of the second-order autocorrelation $g^{(2)}(\tau)$ measurements were analyzed and fitted without background correction unless specified otherwise.

ODMR. The ODMR spectra were measured with a confocal microscope setup. A 100× objective (Olympus MPLN100X) was used to focus a 532-nm laser (LaserQuantum opus 532) onto the sample and collect the PL signal. The PL signal is collected back through a 650-nm short-pass dichroic mirror for separation from scattered laser light. Additionally, a 532nm and 550nm long-pass filter were used before the PL was detected by a silicon avalanche photodiode (Thorlabs APD440A) to filter out the laser light. The microwave field was applied through a signal generator-plus-amplifier system (Stanford Research Systems SG384 + VectaWave VBA1000-18 Amplifier); the sample was placed on a 0.5-mm-wide copper stripline. In order to detect the ODMR signal (i.e. the relative ΔPL/PL contrast) by lock-in technique (Signal Recovery 7230), the microwaves were driven with an on-off modulation. The resonant condition was changed with the external magnetic field by mounting a permanent magnet below the sample.

Raman Spectroscopy. Raman spectroscopy measurements were carried out on an In-Via confocal Raman (Renishaw) system using a 633-nm excitation source. Calibration of the Spectrometer was carried out using a Si substrate to 520 cm^{-1}. The peaks were then fitted to a Lorentzian line profile, from which the corresponding peak center position and full width at half maximum (FWHM) were extracted. Samples were analyzed after transfer to SiO$_2$.

Computational. Many innovative approaches are used in order to model defects with large 3D spatial deformations, as described in detail in Supporting Information. The core elements are the use of Gaussian-16* to perform TD-DFT calculations within a QM/MM model utilizing CAM-B3LYP and an AMBER h-BN force field fitted to mimic CAM-B3LYP. Spectra are simulated with the Huang-Rhys model based on analytically obtained second-derivatives for both ground and excited states.

* Frisch, M. J. *et al. Gaussian 16 Revision C.01.* (Gaussian Inc., Wallingford, CT, 2016).

References

1.   Atatüre M, Englund D, Vamivakas N, Lee S-Y, Wrachtrup J. Material platforms for spin-based photonic quantum technologies. *Nature Reviews Materials* 2018, **3**(5)**:** 38-51.

2.   Lukin DM, Dory C, Guidry MA, Yang KY, Mishra SD, Trivedi R, *et al.* 4H-silicon-carbide-on-insulator for integrated quantum and nonlinear photonics. *Nature Photonics* 2019.

3.   Evans RE, Bhaskar MK, Sukachev DD, Nguyen CT, Sipahigil A, Burek MJ, *et al.* Photon-mediated interactions between quantum emitters in a diamond nanocavity. *Science* 2018, **362**(6415)**:** 662-665.

4.   Tran TT, Bray K, Ford MJ, Toth M, Aharonovich I. Quantum emission from hexagonal boron nitride monolayers. *Nature Nanotech* 2016, **11:** 37-41.

5.   Caldwell JD, Aharonovich I, Cassabois G, Edgar JH, Gil B, Basov DN. Photonics with hexagonal boron nitride. *Nature Reviews Materials* 2019, **4**(8)**:** 552-567.

6.   Exarhos AL, Hopper DA, Grote RR, Alkauskas A, Bassett LC. Optical Signatures of Quantum Emitters in Suspended Hexagonal Boron Nitride. *ACS Nano* 2017, **11**(3)**:** 3328-3336.

7.   Jungwirth NR, Fuchs GD. Optical Absorption and Emission Mechanisms of Single Defects in Hexagonal Boron Nitride. *Phys Rev Lett* 2017, **119**(5)**:** 057401.

8.   Proscia NV, Shotan Z, Jayakumar H, Reddy P, Dollar M, Alkauskas A, *et al.* Near-deterministic activation of room temperature quantum emitters in hexagonal boron nitride. *Optica* 2018, **5:** 1128-1134.

9.   Mendelson N, Doherty M, Toth M, Aharonovich I, Tran TT. Strain-Induced Modification of the Optical Characteristics of Quantum Emitters in Hexagonal Boron Nitride. *Adv Mater* 2020**:** e1908316.

10.   Noh G, Choi D, Kim J-H, Im D-G, Kim Y-H, Seo H, *et al.* Stark Tuning of Single-Photon Emitters in Hexagonal Boron Nitride. *Nano Lett* 2018, **18**(8)**:** 4710-4715.

11.   Nikolay N, Mendelson N, Sadzak N, Böhm F, Tran TT, Sontheimer B, *et al.* Very Large and Reversible Stark-Shift Tuning of Single Emitters in Layered Hexagonal Boron Nitride. *Physical Review Applied* 2019, **11**(4)**:** 041001.

12.   Xue Y, Wang H, Tan Q, Zhang J, Yu T, Ding K, *et al.* Anomalous Pressure Characteristics of Defects in Hexagonal Boron Nitride Flakes. *ACS Nano* 2018, **12**(7)**:** 7127-7133.

13.   Kianinia M, Regan B, Tawfik SA, Tran TT, Ford MJ, Aharonovich I, *et al.* Robust Solid-State Quantum System Operating at 800 K. *ACS Photonics* 2017, **4**(4)**:** 768-773.

14.   Dietrich A, Doherty MW, Aharonovich I, Kubanek A. Solid-state single photon source with Fourier transform limited lines at room temperature. *Physical Review B* 2020, **101**(8).

15.   Konthasinghe K, Chakraborty C, Mathur N, Qiu L, Mukherjee A, Fuchs GD, *et al.* Rabi oscillations and resonance fluorescence from a single hexagonal boron nitride quantum emitter. *Optica* 2019, **6**(5).

16.   Sontheimer B, Braun M, Nikolay N, Sadzak N, Aharonovich I, Benson O. Photodynamics of quantum emitters in hexagonal boron nitride revealed by low-temperature spectroscopy. *Physical Review B* 2017, **96**(12).

17.   Gottscholl A, Kianinia M, Soltamov V, Orlinskii S, Mamin G, Bradac C, *et al.* Initialization and read-out of intrinsic spin defects in a van der Waals crystal at room temperature. *Nature Materials* 2020.

18.   Chejanovsky N, Mukherjee A, Kim Y, Denisenko A, Finkler A, Taniguchi T, *et al.* Single spin resonance in a van der Waals embedded paramagnetic defect. *https://arxivorg/abs/190605903* 2019.

19.   Feng J, Deschout H, Caneva S, Hofmann S, Loncaric I, Lazic P, *et al.* Imaging of Optically Active Defects with Nanometer Resolution. *Nano Lett* 2018, **18**(3)**:** 1739-1744.

20.   Mackoit-Sinkevičienė M, Maciaszek M, Van de Walle CG, Alkauskas A. Carbon dimer defect as a source of the 4.1 eV luminescence in hexagonal boron nitride. *Applied Physics Letters* 2019, **115**(21).

21.   Sajid A, Reimers JR, Ford MJ. Defect states in hexagonal boron nitride: Assignments of observed properties and prediction of properties relevant to quantum computation. *Phys Rev B* 2018, **97**(6)**:** 064101.

22.   Reimers JR, Sajid A, Kobayashi R, Ford MJ. Understanding and Calibrating Density-Functional-Theory Calculations Describing the Energy and Spectroscopy of Defect Sites in Hexagonal Boron Nitride. *Journal of Chemical Theory and Computation* 2018, **14**(3)**:** 1602-1613.

23.   Abdi M, Chou J-P, Gali A, Plenio MB. Color Centers in Hexagonal Boron Nitride Monolayers: A Group Theory and Ab Initio Analysis. *ACS Photonics* 2018, **5:** 1967-1976.

24.   Onodera M, Watanabe K, Isayama M, Arai M, Masubuchi S, Moriya R, *et al.* Carbon-Rich Domain in Hexagonal Boron Nitride: Carrier Mobility Degradation and Anomalous Bending of the Landau Fan Diagram in Adjacent Graphene. *Nano Lett* 2019, **19**(10)**:** 7282-7286.

25.   Chugh D, Wong-Leung J, Li L, Lysevych M, Tan HH, Jagadish C. Flow modulation epitaxy of hexagonal boron nitride. *2D Materials* 2018, **5**(4).

26.   Mendelson N, Xu ZQ, Tran TT, Kianinia M, Scott J, Bradac C, *et al.* Engineering and Tuning of Quantum Emitters in Few-Layer Hexagonal Boron Nitride. *ACS Nano* 2019, **13**(3)**:** 3132-3140.

27.   Stern HL, Wang R, Fan Y, Mizuta R, Stewart JC, Needham LM, *et al.* Spectrally Resolved Photodynamics of Individual Emitters in Large-Area Monolayers of Hexagonal Boron Nitride. *ACS Nano* 2019, **13**(4)**:** 4538-4547.

28.   Wigger D, Schmidt R, Del Pozo-Zamudio O, Preuß JA, Tonndorf P, Schneider R, *et al.* Phonon-assisted emission and absorption of individual color centers in hexagonal boron nitride. *2D Materials* 2019, **6**(3).

29.   Feldman MA, Puretzky A, Lindsay L, Tucker E, Briggs DP, Evans PG, *et al.* Phonon-induced multicolor correlations in hBN single-photon emitters. *Physical Review B* 2019, **99**(2).

30.   Cheng TS, Summerfield A, Mellor CJ, Davies A, Khlobystov AN, Eaves L, *et al.* High-temperature molecular beam epitaxy of hexagonal boron nitride layers. *Journal of Vacuum Science & Technology B, Nanotechnology and Microelectronics: Materials, Processing, Measurement, and Phenomena* 2018, **36**(2).

31.   Hernández-Mínguez A, Lähnemann J, Nakhaie S, Lopes JMJ, Santos PV. Luminescent Defects in a Few-Layer
h
-BN Film Grown by Molecular Beam Epitaxy. *Physical Review Applied* 2018, **10**(4).

32.   de Heer WA, Berger C, Ruan M, Sprinkle M, Li X, Hu Y, *et al.* Large area and structured epitaxial graphene produced by confinement controlled sublimation of silicon carbide. *Proc Natl Acad Sci U S A* 2011, **108**(41)**:** 16900-16905.

33.   Rousseas M, Goldstein AP, Mickelson W, Worsley MA, Woo L, Zettl A. Synthesis of highly crystalline sp2-bonded boron nitride aerogels. *ACS Nano* 2013, **7**(10)**:** 8540-8546.

34.   Schué L, Stenger I, Fossard F, Loiseau A, Barjon J. Characterization methods dedicated to nanometer-thick hBN layers. *2D Materials* 2016, **4**(1).

35.   Orwa JO, Ganesan K, Newnham J, Santori C, Barclay P, Fu KMC, *et al.* An upper limit on the lateral vacancy diffusion length in diamond. *Diamond and Related Materials* 2012, **24:** 6-10.

36.   Breitweiser SA, Exarhos AL, Patel RN, Saouaf J, Porat B, Hopper DA, *et al.* Efficient Optical Quantification of Heterogeneous Emitter Ensembles. *ACS Photonics* 2019, **7**(1)**:** 288-295.

37.   Vogl T, Campbell G, Buchler BC, Lu Y, Lam PK. Fabrication and Deterministic Transfer of High-Quality Quantum Emitters in Hexagonal Boron Nitride. *ACS Photonics* 2018, **5**(6)**:** 2305-2312.

38. Casida ME. Time-dependent density functional response theory for molecules. In: Chong DP (ed). *Recent Advances in Density Functional Methods, Part 1*. World Scientific: Singapore, 1995, pp 155-192.

39. Yanai T, Tew DP, Handy NC. A new hybrid exchange-correlation functional using the Coulomb-attenuating method (CAM-B3LYP). *Chem Phys Lett* 2004, **393**(1-3)**:** 51-57.

40. Heyd J, Scuseria GE, Ernzerhof M. Hybrid functionals based on a screened Coulomb potential. *J Chem Phys* 2003, **118**(18)**:** 8207-8215.

41. Stanton JF, Bartlett RJ. The equation of motion coupled-cluster method. A systematic biorthogonal approach to molecular excitation energies, transition probabilities, and excited state properties. *J Chem Phys* 1993, **98:** 7029-7039.

42. Cornell WD, Cieplak P, Bayly CI, Gould IR, Merz Jr KM, Ferguson DM*, et al.* A second generation force field for the simulation of proteins, nucleic acids, and organic molecules. *J Am Chem Soc* 1995, **117:** 5179-5197.

43. Nikolay N, Mendelson N, Özelci E, Sontheimer B, Böhm F, Kewes G*, et al.* Direct measurement of quantum efficiency of single-photon emitters in hexagonal boron nitride. *Optica* 2019, **6**(8).

44. Korona T, Chojecki M. Exploring point defects in hexagonal boron-nitrogen monolayers. *Int J Quantum Chem* 2019, **119**(14)**:** e25925.

45. Reimers JR, Sajid A, Kobayashi R, Ford MJ. Understanding and Calibrating Density-Functional-Theory Calculations Describing the Energy and Spectroscopy of Defect Sites in Hexagonal Boron Nitride. *J Chem Theory Comput* 2018, **14**(3)**:** 1602-1613.

46. Tran TT, Elbadawi C, Totonjian D, Lobo CJ, Grosso G, Moon H*, et al.* Robust Multicolor Single Photon Emission from Point Defects in Hexagonal Boron Nitride. *ACS Nano* 2016, **10**(8)**:** 7331-7338.